Acoustic waves for active reduction of droplet impact contact time

Mehdi H. Biroun[1], Jie Li[2], Ran Tao[3,1], Mohammad Rahmati[1], Glen McHale[1], Linxi Dong[2], Mehdi Jangi[4], Hamdi Torun[1], YongQing Fu[1,*]

[1] Faculty of Engineering & Environment, Northumbria University, Newcastle upon Tyne, NE1 8ST, UK

[2] Smart Microsensors and Microsystems Engineering Research Center of Ministry of Education, College of Electronics and Information, Hangzhou Dianzi University, Hangzhou, 310018, China

[3] Shenzhen Key Laboratory of Advanced Thin Films and Applications, College of Physics and Optoelectronic Engineering, Shenzhen University, Shenzhen, 518060, P. R. China

[4] Department of Mechanical Engineering, University of Birmingham, Birmingham, B15 2TT, UK

Abstract: Minimising droplet impact contact time is critical for applications such as self-cleaning, anti-erosion or anti-icing. Recent studies have used texturing of surfaces to split droplets during impact or inducing asymmetric spreading, but these require specifically designed substrates which cannot be easily reconfigured. A key challenge is to realise an effective reduction in contact time during droplet impingement on a smooth surface without texturing but with an active and programmable control. Our experimental results show that surface acoustic waves (SAWs), generated at a location distant from a point of droplet impact, can be used to minimise contact time by as much as 35% without requiring a textured surface. Besides, the ability to switch on and off the SAWs means that reduction in droplet impact contact time on a surface can be controlled in a programmable manner. Moreover, our results show that by applying acoustic waves, the impact regime of the droplet on the solid surface can be changed from deposition or partial rebound to complete rebound. To study the dynamics of the droplet impact, we developed a numerical model for the multi-phase flow and simulated different droplet impingement scenarios. Numerical results revealed that the acoustic waves could be used to modify and control the internal velocity fields inside the droplet. By breaking the symmetry of the internal recirculation patterns inside the droplet, the kinetic energy recovered from interfacial energy during the retraction process is increased, and the droplet can be fully separated from the surface with a much shorter contact time. Our work opens up opportunities to use SAW devices to minimise the contact time, change the droplet impact regime and program/control the droplet's rebounding on smooth/planar and curved surfaces as well as rough/textured surfaces.

I. Introduction

Water-repellent materials and surfaces are widespread among plants and animals such as rice/lotus leaves, mosquito eyes, spider silks, fish scales, and red rose petals [1,2]. They have inspired researchers to develop different biomimetic surfaces with extraordinary nonwettability for various applications such as self-cleaning, liquid collection, anti-corrosion, anti-fogging, drag reduction, anti-erosion, anti-icing, and de-icing [3–6].

A droplet bouncing onto a solid water-repellent surface will spread out onto the surface to a maximum contact diameter [7,8] and then retract until it partially wets or completely rebounds and detaches from the surface [9,10]. In this case, surface features such as texture and hydrophobicity play key roles in

* Corresponding author.

Richard.Fu@northumbria.ac.uk

determining the rebounding shapes, patterns and contact time. The period that the droplet is in contact with the solid surface depends on the droplet inertia, capillary forces, volume of the droplet, surface texture/topography, and solid-liquid interaction during spreading and retracting [11]. It is well known that droplet contact time is dominated by the retraction phase rather than spreading phase [12] and is limited by the Rayleigh limit for symmetrical rebouncing [13].

To reduce the droplet retraction time, many studies are focused on changing the symmetrical shape of the droplet during the impingement. A droplet can be split during the impact by a submillimetric ridge/blade on the surface, thus leading to contact time reduction. Bird et al. [14] showed that the symmetry of the droplet impinging on a single ridge on the surface would break and the contact time could be significantly reduced. To do this, they designed a structure with a single ridge and achieved a shorter contact time. Later, Gauthier et al. [15] showed that the droplet contact time on ridged macrostructures takes discrete values when the impact speed is varied. They discussed that depending on impact velocity, a different number of lobes could be shaped during the spreading phase, and the contact time could be reduced by the square root of the number of the lobes. They also designed a Y-pattern ridge on the smooth solid surface to break the droplet into three subunits and found that the contact time (when the droplet was impacted onto the centre of the Y-pattern) was reduced by a factor of $\sqrt{3}$. Similarly, Shen et al. [16] demonstrated that by impacting the water droplet onto cross-shaped blades on the surface, the retraction phase could be merged into the spreading one, and a limited contact time of 5.5 ms can be achieved. Recently, Li et al. showed that by patterning surface wettability, translational motion during retraction could be converted to gyration, thereby creating a rotational rebound [17].

Although the aforementioned methods can decrease the contact time, they are only effective when droplets impact on a certain point on the surface along a certain direction, which presents challenges for their translation into real-world applications. To overcome this issue, different types of macro-structures have been introduced in the literature to reduce the contact time on a larger contact area. A group of researchers focused on fabrication of macro grooves on the solid surfaces to break the droplet symmetry and change the impact behaviour [11,18–22]. For example, Song et al. [21] designed and fabricated an anisotropic grooved surface, and were able to reduce the contact time by ~45% when the distance between the grooves is comparable to the droplet diameter. Recently Guo et al. [22] showed that a droplet impacting on a grooved surface within a certain range of impact velocity could be detached from the surface in a petal-like shape, leading to a reduction of 70% in contact time. Abolghasemibizaki et al. [11] studied the droplet impact on a superhydrophobic surface with cylindrical macrostructures and showed that the retraction time was decreased by the factor of ~$\sqrt{2/\pi}$.

Macrostructure surfaces with designs of different post arrays have also been used to reduce the contact time of bouncing droplets [4,23,24]. For example, Liu et al. [25,26] showed that a droplet would be spread on a surface patterned with arrays of submillimetric truncated pyramidal post arrays and detached from the surface in a pancake shape, leading to a contact time reduction up to ~50%. Later, Song et al. [27] studied the effect of the size of the pillar arrays and introduced a manufacturing method of the superhydrophobic pillar arrays over a large area for pancake bouncing.

Another approach to decrease the contact time is droplet impact on curved smooth surfaces. The droplet symmetry can also be altered by impacting on cylindrically curved surfaces [28–30]. For example, Liu et al. [31] numerically and experimentally investigated the droplet impact on convex/concave surfaces. Their results showed that asymmetric momentum distribution during the impact leads to ~40% contact time reduction compared to the flat surface.

In addition to the efforts to decrease the contact time by changing the solid surface texture and geometry, active methods, such as vibrating the solid surface, have been used. Weisensee et al. [32] investigated the effect of the vibration of the solid surface with frequencies of 60–320 Hz and amplitudes of 0.2–2.7 mm during droplet impact. Their results showed that by vibrating the solid surface at frequencies higher than 100 Hz, the contact time could be decreased by 50%.

The need for manufacturing a textured surface with macrostructures or vibrating whole structure brings complexity especially at large a scale for practical applications. It is, therefore, crucial to find new methodologies to manipulate droplet impact on a smooth and non-textured surface with a large area coverage. In this study, we hypothesize that the contact time of an impacting droplet might be reduced by remotely generating surface acoustic waves (SAWs), which then propagate along a smooth and non-textured surface into the area where the droplet impact is occurring. For the experimental investigation, we designed and fabricated thin-film SAW devices to apply wave energy into the droplet during its impingement process. We discovered it is possible to reduce the contact time up to 35% by applying a SAW along one side of the droplet, whereas the reduction is only by ~10% when the SAW is applied along with two opposing directions with the same amplitude. Furthermore, results showed that the droplet impact regime could be effectively changed from droplet deposition on the surface to fully rebounding by using SAWs. Using these insights, droplet impingement properties such as contact time and rebouncing angle can be programmed and controlled electrically.

To understand the underlying physics of these phenomena, we developed a numerical method and simulated the droplet impact process with and without SAW actuation. After validation of the method with experimental results, we compared the numerical results for different scenarios of droplet impact. High fidelity numerical results showed that there are apparent differences in internal streaming patterns of the droplet during the impact, which lead to higher kinetic energy, vertical momentum and less viscous dissipation inside the droplet subjected to SAW power-driven from one side, compared to those for the droplet driven from both sides. As a result, the droplet is separated from the surface slightly slower in the latter case.

II. Design and Theoretical analysis

SAW-based microfluidics (acoustofluidics) has recently found many applications in lab on a chip [33–35] tissue engineering [36], biology and medicine [37–39]. SAWs can be generated by applying a radio frequency (RF) signal to interdigital transducers (IDTs) which are patterned on a piezoelectric substrate. When the propagating SAWs reach a liquid medium on the substrate, depending on their amplitudes and frequencies as well as properties of liquid and piezoelectric substrate material, their momentum is transferred inside the liquid along the Rayleigh angle ($\theta_R = sin^{-1} v_L/v_S$, where v_L and v_S are the sound velocity in liquid and solid medium respectively) [40]. Different droplet actuation phenomena as a result of the transferred momentum, including mixing, pumping, jetting and atomisation by SAW have been extensively investigated over the last two decades [40]. Generation of leaky SAWs at the interface of liquid and solid surfaces affects the internal streaming patterns inside an impinging droplet, thus can lead to breaking the symmetry of patterns and result in a potential reduction of the droplet impact time. The momentum transferred by a SAW to a droplet can be described using a body force which is applied to the liquid medium along the Rayleigh angle by [41,42]:

$$F_{SAW} = -\rho(1 + {\alpha_1}^2)^{3/2} A^2 \omega^2 k exp\,(2[kx + \alpha_1 kz]) \qquad (1)$$

where A and ω are the wave amplitude and frequency, k is the imaginary part of k_L which is the wavenumber of the leaky surface acoustic waves (LSAWs). $\alpha_1 = \sqrt{(v_S/v_L)^2 - 1}$ is the attenuation constant. FIG. 1 illustrates the droplet impingement dynamics on the solid surface in the presence of a propagating SAW. The droplet contact width is characterised by $\beta = \delta/D_0$, which is the ratio of the contact width, δ, to the initial droplet diameter, D_0. We expect to observe the droplet interface asymmetry along the x-axis, which would be triggered by the conversion of SAW energy into the LSAWs and the resulting different internal streaming patterns inside the droplet. This would affect the various interfaces, which in turn could lead to a different contact widths and dynamics during the impingement. It is reasonable to conjecture that the droplet may detach from the surface sooner and along a non-normal detachment angle, as shown in Fig. 1.

Based on the above hypothesis, in this study, we aim to determine whether the contact time will be reduced by applying the SAW during the droplet impact on the solid surface. To achieve this, we used a thin-film ZnO/Si SAW device with a resonant frequency of 66.2 MHz. We used two types of designs in this study, including (1) travelling surface acoustic

waves (TSAWs, i.e., with waves propagating from IDTs along one side of the droplet), and (2) standing surface acoustic waves (SSAWs, i.e., two waves propagating from IDTs along the two opposite sides of the droplet) during droplet impingement. The experimental results were compared with the conventional droplet free impact (DFI) on the solid surface in terms of contact width and contact time as functions of SAW amplitude and the Weber number ($We = \rho {U_0}^2 D_0/\gamma$, in which ρ, U_0, D_0, γ are density, impact velocity, initial diameter, and surface tension of the droplet, respectively).

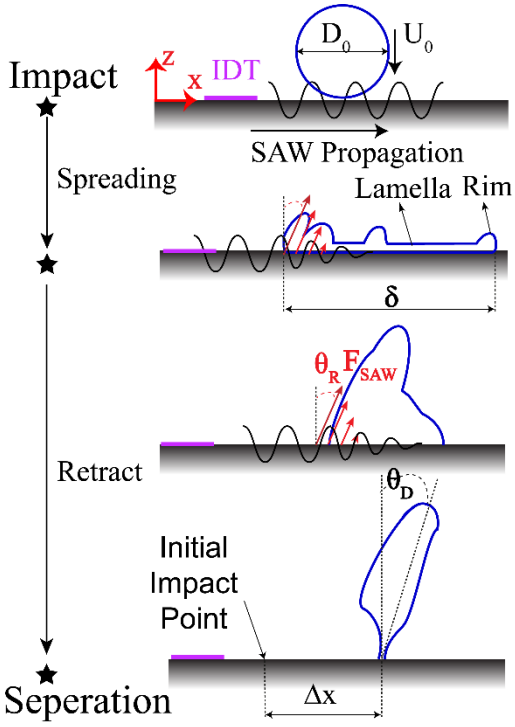

FIG. 1: Anticipated time evolution of droplet impact on a solid surface with the presence of SAW propagating on the surface. SAWs can dissipate energy into the liquid droplet during its impact process and break-off the symmetry in droplet spreading and retracting phase leading to shorter contact time.

III. Materials and Methods

A. SAW device preparation

ZnO films with a thickness of 5 μm were deposited onto (100) silicon wafers and aluminium plates using a direct current magnetron sputter system (NS3750, Nordiko). The vacuum of the sputter chamber was maintained at ~0.35 Pa during the deposition with an Ar/O_2 flow ratio of 3/11. The Cr/Au IDTs with the thickness of 20/100 nm were fabricated onto the ZnO/Si and ZnO/Al substrate using a standard photolithography and lift-off process. The bi-directional IDTs consist of 30 pairs of fingers, with an aperture of 5 mm and spatial periodicities of 36-200 microns. To obtain a hydrophobic surface, the surface of the SAW device was coated with a hydrophobic CYTOP (Asahi Glass Co.) layer. To measure the resonant frequency and the amplitude of the SAW device, an HP8752A RF network analyser was used. The generated Rayleigh wave by a signal generator (Marconi 2024, Plainview, USA) was amplified using an RF power amplifier (Amplifier research, 75A250, Souderton, USA) before applying to the IDTs. The measured resonant frequencies of the fabricated ZnO/Si SAW devices and calculated velocities are listed in **Error! Reference source not found.**. To convert the applied power to the non-dimensional SAW amplitude, the equation proposed by Alghane et al. was applied [43]

$$\frac{A}{\lambda} = 8.15 \times 10^{-6} {P_{RF}}^{0.225} + 5 \times 10^{-6} {P_{RF}}^{0.8} \qquad (2)$$

where λ is the wavelength of the SAW in meter, and P_{RF} is the applied power to SAW device in Watts.

B. Droplet bouncing and imaging

Droplets of deionised water, with a density of $\rho = 995\ kgm^{-3}$ and surface tension $\gamma_{LV} = 72 \times 10^{-3}\ Nm^{-1}$ at 21 °C with volumes between 3.56 and 5.84 μl were generated by squeezing the nozzle until the droplet is detached under its gravity from the edge of a needle (BD Microlance). For each needle, the droplet size was calculated using the approach proposed by Aminzadeh et al. [44] and was repeatable with <5%. By adjusting the drop height, the impact velocity was varied between 1.4 and 2 m/s. The impact process was filmed from side-view using a high-speed Camera (HotShot 1280CC) at 5000 fps. Droplet contact time, τ, was defined for all the cases between the first touch of the droplet to the surface and when the water is separated from the substrate. The SAW was applied just before the droplet detachment from the needle to skip the temperature raise in the solid surface. The temperature of the

surface was maintained to the lab temperature (21 °C) in all the cases. Each impact was repeated three times to ensure the repeatability of the experiment. Table I lists the measured data for the SAW devices.

C. Numerical method

To numerically investigate the impact cases, an interface capturing method based on the coupled level-set volume of fluid (CLSVOF) method was developed using an OpenFOAM 4.x. Open-source toolbox. The CLSVOF method was used to capture a sharp and smooth liquid/gas interface and conserve the mass during the calculation [45,46]. The developed code is capable of 3D simulation of unsteady droplet interaction with the solid surface in the presence of SAW. To optimise the computational costs, the impact was simulated by three different mesh domains. The droplet was released from a height of 10 cm from the surface, which was simulated by a rectangular mesh with a dimension of $3.2 \times 3.2 \times 102.0\,(\mathrm{mm})$ consisting of 3,525,120 hexahedral cells. Then the CFD fields after 150 ms were mapped to a new rectangular mesh with a dimension of $7.0 \times 7.0 \times 3.0\,(\mathrm{mm})$ consisting of 3,786,444 hexahedral cells to simulate the spreading and retracting phases. Finally, to simulate the detachment phase, another rectangular domain with dimensions of $3.0 \times 3.0 \times 6.0\,(\mathrm{mm})$ consisting of 3,456,000 hexahedral cells was used. The mesh resolution of the drop was 35 cells per diameter. Variable time step with a maximum Courant number of 0.3 was chosen to keep the normalized residuals to be less than 10-5. A dynamic contact angle model was developed to capture the spreading and retracting dynamics accurately (see equation 7 in Appendix D). Partial slip velocity boundary condition based on Afkhami et al.'s [47] Model was developed and used for the solid surface.

IV. Results

A. Experimental results

As explained in the Experimental section, different SAW devices on different substrates with resonant frequencies ranging from 22.04 to 110.84 MHz were designed and fabricated to investigate the droplet impact hydrodynamics in the presence of SAWs. Effects of SAW device substrate (i.e. on the generation of different Rayleigh angles) and IDT design (i.e. achieving the different resonant frequencies) are shown in Appendix A and B, respectively. Based on these results, we selected the ZnO/Si SAW device with a resonant frequency of 66.10 MHz for further studies. FIG. 2 (a-c) show snapshots of the droplet impact images on the SAW device surface with the CYTOP surface treatment for three different cases of DFI, TSAW, and SSAW, respectively. When the droplet impinges onto the solid surface in both the cases of DFI and SSAW, it starts to spread into its maximum diameter before it starts to retract, and both the deformation patterns are quite symmetric with respect to the z-axis. Whereas the TSAW shows a more irregular and asymmetric pattern (see Fig. 2(b)), which is more significant during its maximum spreading and retraction/ detachment periods. **Error! Reference source not found.**(a) shows comparisons between experimental and simulation results as a function of the normalized contact width for all three impact cases. During the spreading and retracting stages (e.g., t < 6 ms), the dynamics are comparable for these three cases. The spreading time (τ_s) for all the cases is similar and can be given as $\tau_s/\tau \sim We^{-0.5}$ [48]. The contact time for the TSAW case is reduced by ~4.6 ms compared with the DFI case, mainly due to the shortening of the detachment period in this case. **Error! Reference source not found.**(b) shows the maximum contact width for both the TSAW and SSAW cases at different SAW amplitudes (i.e. different RF powers applied to the IDTs). By increasing the SAW amplitude, the maximum spreading diameter is decreased. As expected, this radius reduction during the impact is higher for the SSAW case, as the x-component of the SAW force from both directions restrain the contact line movement during its spreading phase.

Error! Reference source not found.(c) shows the normalized contact time of the droplet versus SAW amplitude. For the TSAW cases, the contact time is reduced by increasing the SAW amplitude. Whereas at lower SAW amplitudes ($A/\lambda < 3\times10^{-5}$), the reduction percentage of the contact time is not significant, due to the lower energy transferred from the solid surface during the impingement. By increasing the normalized SAW amplitude up to 1.2×10^{-4}, the contact time is significantly reduced by ~25%. For the SSAW case, the evolution of the contact time can be divided into two stages. The contact time reduction is observed at normalized

amplitudes lower than 7×10^{-5}, whereas the contact time is increased at normalized amplitudes higher than this value.

Table I: Resonant frequency, Rayleigh angle, CT, static contact angle (SCA), advancing contact angle (ACA), receding contact angle (RCA) and contact angle hysteresis (CAH) for ZnO/Si SAW device with and without surface treatment. In this table, ± sign shows the standard error.

SAW Device	Resonant Frequency	Rayleigh Angle	α_1	θ_s	θ_{adv}	θ_{rec}	$\Delta\theta = \theta_{adv} - \theta_{rec}$
CYTOP/ZnO/Si	66.1 (MHz)	21.2°	2.47	122º±2º	123º±2º	95º±4º	28º±6º
ZnO/Si				86º±3º	90º±4º	27º±4º	63º±8º

The contact time for the DFI scenarios is not a function of impact velocity [49,50]. Interestingly, our experimental results showed that there is a threshold of droplet impact velocity for a complete rebound from the hydrophobic and non-textured surface. As shown in **Error! Reference source not found.**(d), with the impact velocities lower than 1.26 m/s, the initial kinetic energy of the droplet is not high enough to detach the whole droplet from the surface at the end of the retract phase. Supplementary video 1 shows a rebound case with an impact velocity of 1.4 m/s and supplementary video 4 shows a deposition case with an impact velocity of 1.08 m/s. The results in **Error! Reference source not found.**(d) show that by applying the TSAW, impact regime can be effectively changed from deposition to rebound for impact velocities lower than 1.26 m/s. Furthermore, for higher impact velocities, applying the TSAW can reduce the contact time by ~25% on average. The results in **Error! Reference source not found.**(d) indicate that the contact time of the droplet regardless of the presence of SAW is not a function of impact velocity. Results in **Error! Reference source not found.**(d) show that the TSAW can change the nature of the untextured hydrophobic surface into a water repellent surface. The effect of the droplet volume on the impact behaviour is presented in Appendix C.

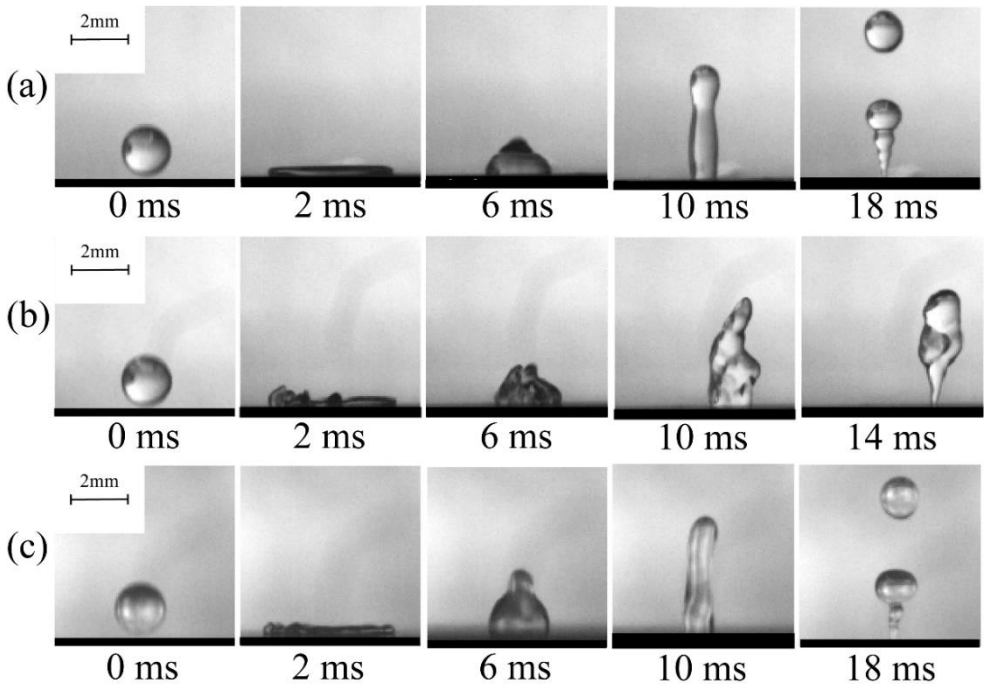

FIG. 2: Experimental snapshots of a water droplet impinging on the solid surface. (a) Droplet free impact case without SAW applied, (b) impact on ZnO/Si surface with TSAW applied to propagate from left to right (c) impact on ZnO/Si surface while SSAW is applied to the surface. For all the experiments, the droplet impact velocity and volume are 1.4 m/s and 3.56 µl. See Supplementary videos 1-3 for experimental movies.

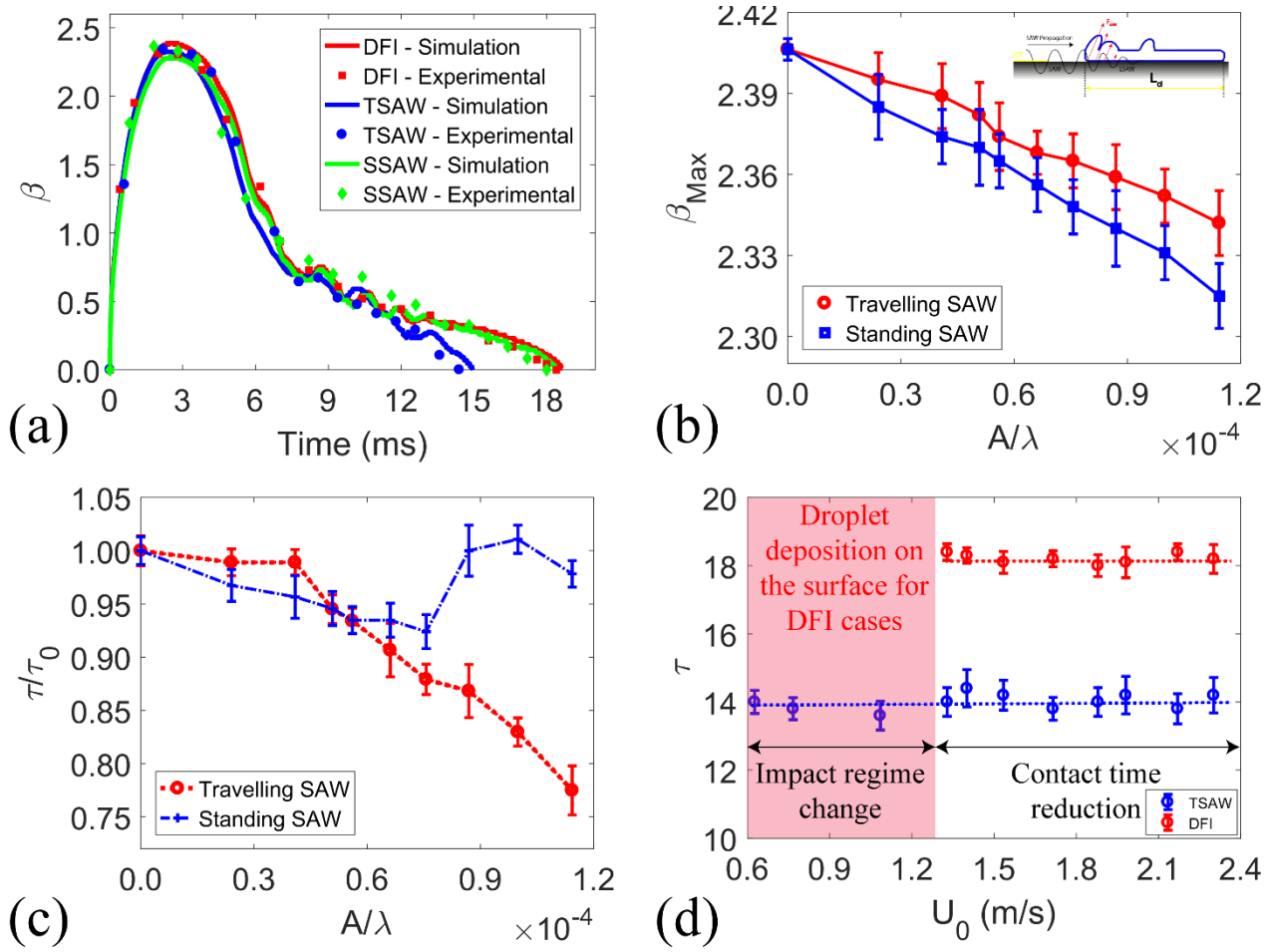

FIG. 3: (a) A comparison between numerical and experimental results for normalized contact width of droplet impact on SAW device for DFI, TSAW and SSAW scenarios. (b) Maximum contact width versus SAW amplitude for both SSAW and TSAW cases. Impact experiments are carried out for a droplet with a volume of 3.56 µl and an impact velocity of 1.4 m/s. (c) Normalized contact time as a function of SAW amplitude for a droplet with a volume of 3.56 µl and impact velocity of 1.4 m/s impacting on the ZnO/Si SAW device surface with CYTOP surface treatment. (d) Contact time versus impact velocity for a droplet with a volume of 3.56 µl for DFI and TSAW scenarios. The shaded area represents droplet deposition on the surface for DFI cases. In all figures, error bars represent SD of the results.

To investigate effects of surface treatment and wettability on the impact dynamics, droplet impact tests with a volume of 3.56 µl and an impact velocity of 1.08 m/s were carried out on the surfaces with and without CYTOP treatments. Same experiments were repeated in the presence of TSAW with a normalized amplitude of ~8.7×10-5 (i.e. RF power of 27 W applied to the IDTs) for both types of the SAW devices. The differences in contact angles of the devices after the surface treatments are listed in Table I.

During the motion of the three-phase contact line (TPCL) on the solid surface, contact angle hysteresis, $\theta_{adv} - \theta_{rec}$, (CAH) generates a force which resists the droplet motion and dissipates the kinetic energy of the droplet. To explain the effect of contact angles on droplet impact hydrodynamics, we focus on the analysis of the work done by this resistive force, W_R, which can be written as [50,51]:

$$W_R \propto \frac{cos\theta_{rec} - cos\theta_{adv}}{1 - \cos\theta_{adv}} \quad (3)$$

Equation (3) shows that during the impact, a higher advancing contact angle (ACA) or a lower CAH can lead to a lower energy dissipation during the TPCL motion.

For the DFI case, due to large work generated by resistive force on the surface without hydrophobic treatment, the droplet still stays on the surface after the impact. In the same DFI case, by treating the surface of the device with a layer of CYTOP, the CAH is decreased by ~35° while the ACA is increased by ~35°, thus resulting in a reduction of resistance work by 320%. Thus, a much lower value of kinetic energy loss by the CAH resistive force can be expected for the CYTOP coated surfaces, and partial rebound of the droplet is observed for the DFI cases on these surfaces (see the supplementary videos 4 and 5 and also the experimental snapshots shown inFIG. 4). Due to the lower energy dissipation by the CAH resistance work, a sub-unit of the liquid has enough energy at the end of the retraction phase to overcome the surface tension and is separated from the droplet while the bulk droplet still remains on the surface.

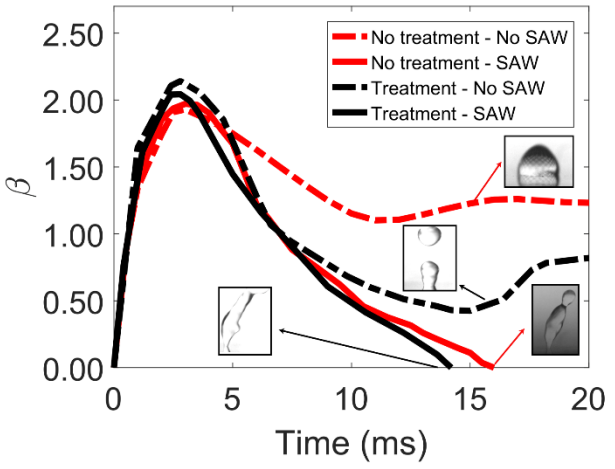

FIG. 4: Temporal evolution of contact width for droplets impacting on the SAW device surface with different wettability. In these experiments, a droplet volume and impact velocity are kept constants at 3.56µl and 1.08 m/s respectively. For each surface coating, experiments are carried out for both DFI and TSAW scenarios. The applied RF power to the IDTs for the TSAW scenario is 27 W. Snapshots of the experimental results confirm that TSAW changes the droplet deposition (red dashed line) and break-up (black dashed line) on the surface to complete rebound (solid lines).

However, for both the treated and non-treated surfaces, by applying the TSAW the droplet gains enough kinetic energy during the impingement to bounce off the surface, mainly due to the large vertical SAW momentum dissipated into the liquid by the z-component of the SAW force (see supplementary videos 6 and 7 and also TSAW experimental snapshots on FIG. 4). As shown in FIG. 4, in the absence of SAW, the droplet stays on the surface at the end of the retraction phase. However, by applying the SAW, the droplet gains more energy during the impingement and is fully separated from the surface. Due to the lower energy loss induced by the resistive work for the surface with CYTOP coating, less kinetic energy is dissipated, thus leading to a faster detachment of the droplet from the surface. FIG. 4 shows that regardless of the surface treatment, applying a TSAW can significantly reduce the contact time. Moreover, the droplet impact regime can be changed from deposition on the surface to complete rebound from the surface after applying the SAW.

B. Numerical simulations

To gain a better insight of the physics of contact reduction by the SAW and to interpret the differences of droplet detachment for both the TSAW and SSAW cases, we further analysed the effect of the SAW on the impingement dynamics using the numerical simulations. An interface capturing method based on the coupled level-set volume of fluid (CLSVOF) method was developed in OpenFOAM 4.x. Open-source toolbox, and used to capture a sharp and smooth liquid/gas interface and conserve the mass during the calculation [52,53]. A series of validation simulations were performed to reproduce the experimental results and test the capability of the developed numerical method. Agreements between the experimental and simulation results are achieved, which can be seen from the results shown inFIG. 3(a).

More details about the numerical method can be found in Appendix D. For the simulation results; we focus on the internal streaming patterns inside the droplet during its spreading and retraction stages to understand the mechanism by which different SAW modes change the contact time. As can be seen inFIG. 5, while the velocity vectors for the DFI and SSAW cases demonstrate rather regular and symmetric flow patterns, the results for the TSAW case (see FIG. 6) involve an irregular flow pattern and a strong internal recirculation on the left-hand side.

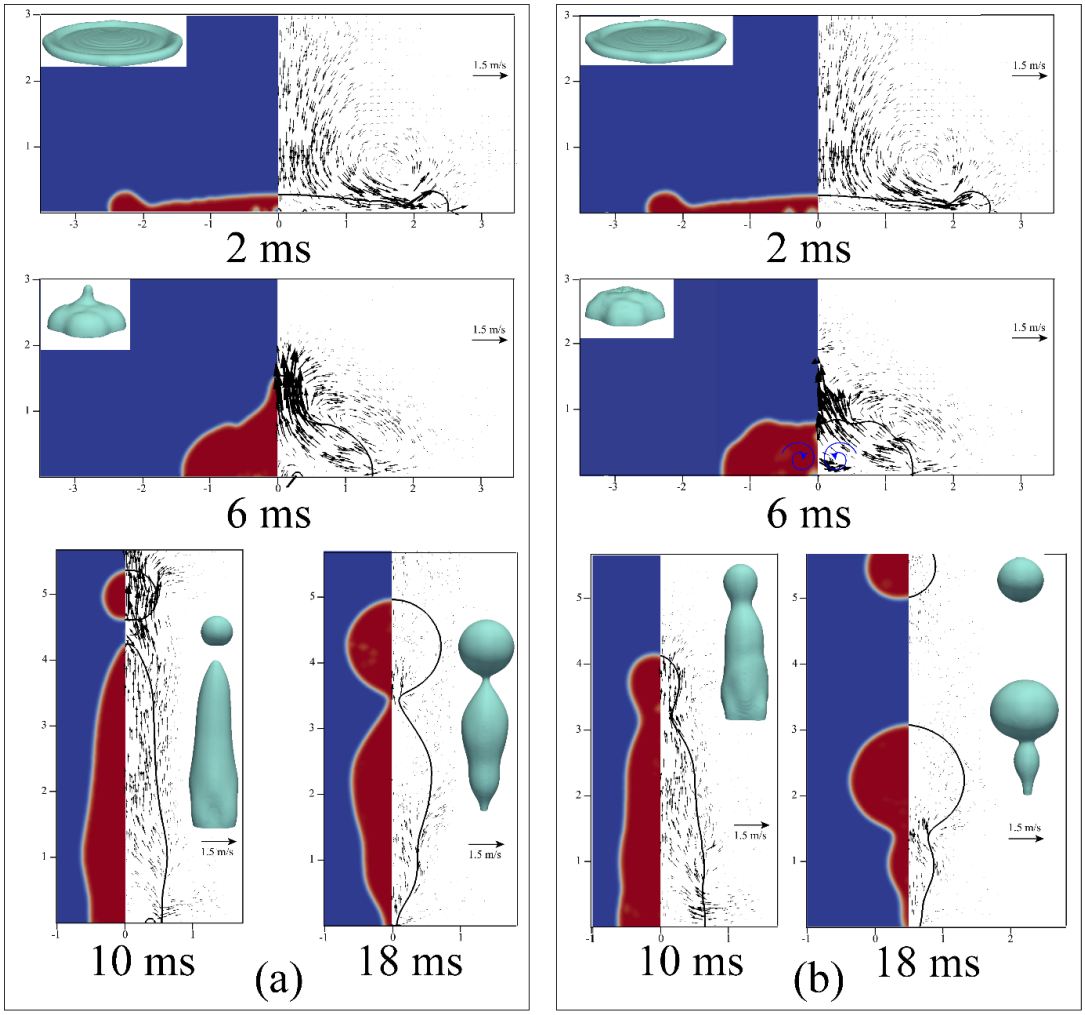

FIG. 5: Time evolution images of the droplet impact dynamics obtained by numerical simulation. (a) DFI scenario. (b) SSAW propagation on the solid surface during the impact. In all the simulations, the droplet impact velocity and volume are 1.4 m/s and 3.56 µl subsequently.

As the process evolves in time, relatively regular flow patterns for both DFI and SSAW cases are developed. It is worth mentioning that both the DFI and SSAW cases exhibit a very similar spreading flow pattern with an almost identical maximum spreading diameter of 2.4 mm, while the apparent differences between these two cases are only observed at a much later stage, e.g., after 6 ms, which is during the retraction period. The case for the TSAW, however, shows very different behaviour. Considering the shape of the interface in FIG. 6 at a time of 3 ms, we notice the initiation of an asymmetric deformation at the interface near the rim in the left-hand side (where it is subjected to the SAWs). This deformation is not present on the right-hand side of this case, neither can be found in the

results for DFI and SSAW cases. The same asymmetric deformation can be seen inFIG. 2(b). This irregular deformation at the droplet interface, which has been initially triggered by the one-sided SAW at 2.5 ms during the spreading period, is rapidly developed during the retraction phase of the droplet impact. The asymmetric retraction of the droplet, in turn, creates even more irregular deformations and instabilities at the interface and rapidly develops an asymmetric flow pattern with a dissimilar interface morphology as it can be seen in FIG. 6 after 7 ms.

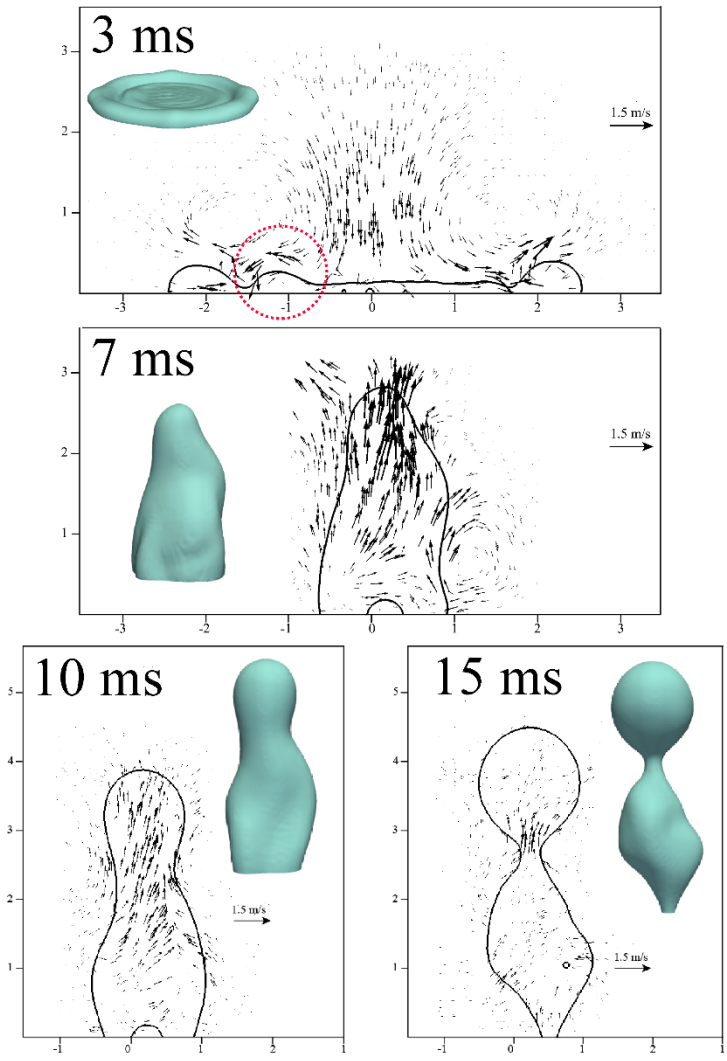

FIG. 6: CFD snapshots of liquid phase overlaid by velocity vectors during the impingement process in the presence of TSAW propagating from left to right. The droplet impact velocity and volume are 1.4 m/s and 3.56 µl subsequently.

During the impingement process, there are continuous changes of gravitational, kinetic and the liquid-vapor-solid interfacial/surface energies. Furthermore, these energies are continuously dissipated during the impact because of viscous dissipation, wave generation on the interface and sub-unit separation [54,55]. We further analysed the energy budget and the rates of conversion of the initial energy of the droplet, E_0, into the kinetic energy, potential energy and interfacial energy in order to reveal the real mechanism of contact time reduction in the TSAW case. The total

interfacial/surface energy of the solid-liquid-vapor system (E_{Interf}) for a droplet in contact with the substrate can be given by

$$E_{Interf} = \gamma_{LV} S_a + (\gamma_{SL} - \gamma_{SV}) S_s + \gamma_{SV} S_\infty \quad (4)$$

where γ_{SV}, γ_{SL} and γ_{LV} are the interfacial tensions (i.e. surface energies per unit area) of the solid-vapor, solid-liquid and liquid-vapor interfaces, respectively. S_a and S_s are the areas of the droplet interfaces in contact with air and solid, and S_∞ is the area of the solid surface in contact with the gas phase in the absence of a droplet. Here the changes in interfacial energy associated with droplet spreading can be defined as $E_D = E_{Interf} - \gamma_{SV} S_\infty$, which sets the reference interfacial energy, E_D, equal to the droplet surface energy at the instant of droplet impact on the surface.

We define the sum of the kinetic, E_K, gravitational energy, E_G, and the interfacial energy associated with droplet spreading, E_D, as the total energy of the droplet:

$$E = E_K + E_G + E_D \quad (5)$$

where E_G is defined as the volume integral of the infinitesimal volume element V potential energy through the liquid phase.

$$E_G = \int \rho_l g z dV \quad (6)$$

where g is the gravitational acceleration, ρ_l is the liquid density and z is the distance in the vertical direction from the solid surface. The kinetic energy E_K is defined as below:

$$E_K = \int \frac{1}{2} \rho_l u^2 dV \quad (4)$$

Here u is the magnitude of the liquid velocity. The time evolution of the energies during the impingement process is shown in FIG. 7. All the energies are normalized by initial droplet total energy, $E_0 = (\rho_l . V_0 . g . H_0 + \gamma_{LV} S_0)$, where H_0, S_0 and V_0 are the droplet initial release height, spherical surface area and volume.

The normalized total energy of the droplet during the impingement, E/E_0, is illustrated inFIG. 7(a). Interestingly, more than 70% of the total energy is dissipated within less than 0.5 ms after the onset of impact, which is consistent with the finding in references [54,56,57]. Since the potential energy is one order of magnitude smaller than kinetic and interfacial energy in eq. (5), it is not shown in FIG. 7.

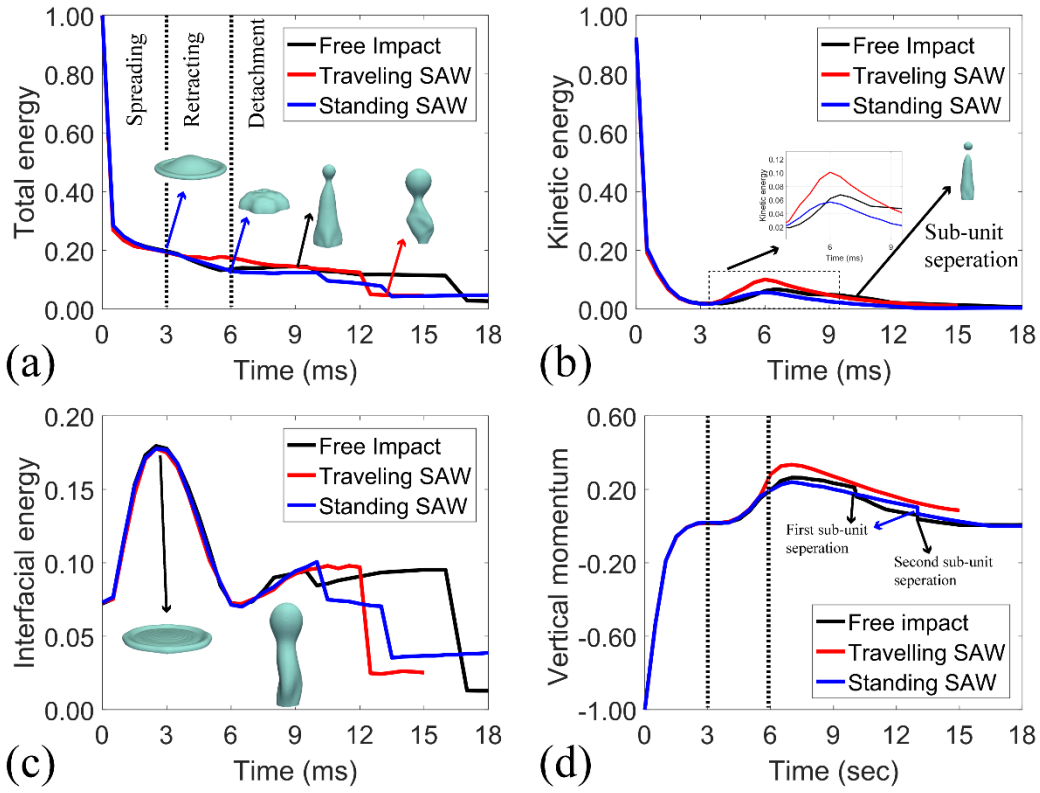

FIG. 7: (a) Total energy, (b) Kinetic energy, (c) Interfacial energy for FI, TSAW, and SSAW scenarios. In the simulation, the droplet impact velocity and volume are 1.4 m/s and 3.56 µl subsequently. All the energies are normalized by kinetic energy at the onset of impact.

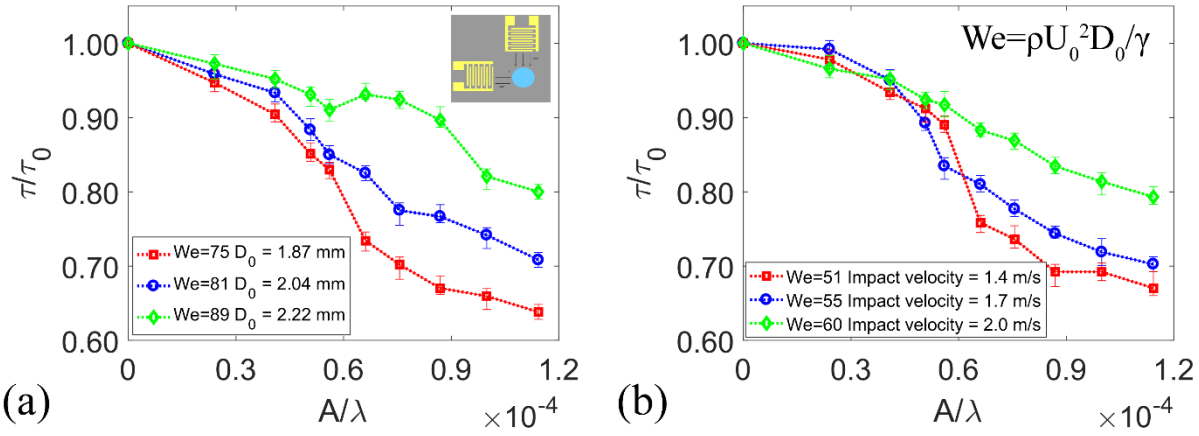

FIG. 8: (a) Experimental results of normalized contact time as a function of SAW amplitude for droplets with the initial diameter of 1.87, 2.04 and 2.22 mm. Impact velocity for all the cases is kept constant at 1.7 m/s. (b) Experimental results of normalized contact time as a function of SAW amplitude for droplets with impact velocities of 1.4, 1.7, and 2.0 m/s. Droplet initial diameter is kept constant at 1.87 mm for the experiments presented in this graph. Error bars represent SD of contact time.

The variation of kinetic energy, E_K (normalized by E_0) shown in FIG. 7(b), indicates its significant reduction in the first 0.5 ms of the impact time. Results in FIG. 7(c) shows only 10% of the kinetic energy is stored in the form of interfacial energy during the spreading phase, and the rest of the kinetic energy is dissipated during the first 0.5 ms of impact. The stored interfacial energy at the end of the spreading phase starts to be converted into kinetic energy and causes the retraction. The conversion of the interfacial energy into kinetic energy leads to an increase in the kinetic energy between 3-6 ms after the onset of the impact. This increase in the kinetic energy is more significant for the TSAW scenario since the kinetic energy is increased both by interfacial energy conversion and applied SAW energy. However, for the SSAT and DFI scenarios, due to the symmetry of droplet deformation, a rather strong internal recirculation field is created within the droplet which dissipates the kinetic energy.

More importantly, FIG. 7(a-c) show that the energy conversion rates for all the cases during the spreading and retracting time, e.g., time < 6 ms, are almost identical. This implies that dissipation of the total initial energy by viscous liquid and interaction between liquid and solid surfaces are the two dominant processes during the initial 6 ms. However, the differences between these cases begin to appear in the values of kinetic energy, after approximately 3.5 ms, because of the presence of SAW, which is shown in the magnified diagram in FIG. 7(b). For example, the recovery rate of the kinetic energy from the interfacial energy between the durations of 3.5 ms and 6 ms, is ~37% higher for the TSAW case compared to that of the SSAW case. The normalized vertical momentum of the droplet by the initial droplet momentum is shown in FIG. 7(d). The differences in the kinetic energy, in turn, increases the vertical momentum of the droplet during the retraction phase. Also, the separation of each sub-unit from the main droplet leads to a sudden decrease in the momentum, which delays the droplet detachment from the surface.

Another interesting phenomenon obtained from FIG. 7(c) is that while significant differences of the variation of kinetic energy between TSAW with those of SSAW and DFI are observed, the interfacial energy in all the cases is almost identical during the spreading and the retraction phases. This clearly shows that the dissipation rate for the TSAW case during the retraction period is 50% smaller than those of SSAW and DFI cases. Snapshots in shown in FIG. 5 (a-b) reveal the mechanism responsible for such higher dissipation rates in the cases of SSAW and DFI. It can be seen in FIG. 5(a-b) at 6 ms that the rather symmetric small-scale vortices have been formed for both the SSAW and DFI cases. Such small-scale vortices have not formed in the TSAW case due to its asymmetric and irregular flow patterns. It is well known that the viscous dissipation rate is exponentially proportional to the inverse of the vortex length scale [58]. Therefore, the conversion of interfacial energy during the retraction period for the TSAW case occurs with a much lower dissipation rate, owing to the absence of such vortices, which in turn leads to a much higher energy conversion efficiency and much larger kinetic energy and vertical momentum inside the droplet during the retract phase.

All the above results indicate that most energies in the SSAW and DFI cases during the retraction processes are dissipated by the symmetric and very stable internal flow recirculation. Whereas they have been recovered into the kinetic energy more efficiently in the TSAW case since such an internal recirculation cannot be easily formed due to the asymmetric and the instabilities. This, in turn, leads to a much faster retraction and dispatching processes of the droplet from the surface in this TSAW case. Simulation results show that by increasing asymmetry in the flow inside the liquid, a shorter contact time can be achieved during droplet impact under the TSAWs.

To further verify this idea, we examined the droplet impact dynamics using a sample with a perpendicular IDT design, which can generate two waves propagating in vertical directions into the droplets (see FIG. 8). Three different cases were tested, and the results are illustrated inFIG. 8(a). Depending on the droplet size, the contact time can be reduced between 20-35%, if compared with the DFI case. Unlike the SSAW cases, in this IDT design, the applied SAWs from both sides create a kinetic energy field that breaks the symmetry of droplet deformation in both X and Y directions and speed-up the detachment process of the bouncing droplet. FIG. 8(b) shows the effects of the impact velocity for the droplet impact dynamics. At lower SAW amplitudes, the contact times for all the cases do not show

significant differences. However, at normalized SAW amplitudes greater than 7×10^{-5}, the contact time is considerably reduced with the increase of the impact velocity. This is mainly due to the significant increase of the acoustic wave energy absorbed by the droplets. Results clearly confirm our prediction that by breaking the droplet symmetry along both X and Y axis, the contact time can be significantly reduced. However, the contact time reduction achieved using this method is limited by the applied power to the IDTs. Applying powers higher than 50 W could damage the SAW device, and at such higher powers, droplet tends to break-up or splash during the spreading phase. In this paper, we only consider the cases in which a complete rebounce is observed.

V. Discussion

Overall, our results clearly indicate that the droplet impact dynamics can be modified and controlled using the thin-film based SAW technique. The key features of the thin-film piezoelectric platform are its seamless, scalable, and localized generation of SAWs, which can then propagate across entire structural surfaces. Piezoelectric films can be deposited and applied locally on a component to generate vibrations, without the need for covering the whole structure surface with the piezoelectric film. The SAW direction and amplitude can also be controlled through electrode shapes and designs, and SAWs can also be generated wirelessly and remotely. Therefore, due to its high efficiency and wireless function, the SAW technique can be used in different engineering applications.

As shown in Fig. 4, a SAW can change the impact regime; thus, a potential application of this technology could be switching a nontextured surface to water-repellent in various structures, such as solar panels surface or vehicle (or airplane or train) windows. Additionally, for the applications in which it is desirable to minimize the interaction between solid and liquid to avoid surface erosion (for instance, wind turbine blades), this method can effectively be used. Moreover, the ability to clean and remove the impacting liquid droplet makes it possible to fabricate anti-contamination/ anti-bacteria surfaces using this method [40,60,61]. The ability to reduce the contact time of the droplet can also be used to control the heat transfer between solid and liquid, or for de-icing and anti-icing applications in airplane wings or wind turbine surfaces. On the other hand, for spray cooling applications such as spray cooling of nuclear reactors [62] and electronic components [63], it is desirable to control the contact time and area of the droplet with the high-temperature surface to regulate the heat transfer rate, and the method we proposed in this study could be suitable for such spray cooling applications.

VI. Conclusion

In this study, we studied the bouncing behaviour of the bouncing droplet under the influence of SAW. Our experimental and numerical results showed that using this novel method droplet contact time can be significantly reduced on the solid surface without changing the solid surface texture or geometry. The SAW can effectively reduce the contact time by up to 35% when travelling SAW is applied to the droplet. We have achieved both vertical and asymmetric rebounds and reduction of contact time without fabricating textured surfaces. Moreover, our results showed that by applying SAW to the droplet, the impact regime could be modified, and droplet deposition on the surface can be effectively avoided by applying SAW to an impacting droplet to achieve a complete rebound from the surface. Simulation results showed that the internal streaming patterns for both the droplet free impact and standing SAW cases are almost symmetrical. On the other hand, applying the travelling SAW creates irregular flow field which breaks the symmetry of the internal streaming and can reduce the contact time. For the droplet free impact and standing SAW cases, the vortices which are created during the retract phase dissipates the kinetic energy more than TSAW, leading to a more contact time before droplet separation from the surface. Since SAWs can be generated remote from a drop impact location and can be switched on and off, this new concept allows the rebound properties of droplets including contact time, bounce angle, and maximum spreading width, to be controlled regardless of the impact point. Importantly, surface acoustic waves can be propagated across large areas of a surface of interest, which can be planar or curved and made of many different types of materials. The approach removes the need to texture or shape a surface to achieve reduced droplet impact time. We, therefore, believe SAW-based droplet impact modification offers a new paradigm for controlling droplet impact

in applications, such as anti-icing, self-cleaning and anti-erosion.

I. Acknowledgements

This work was financially supported by the UK Engineering and Physical Sciences Research Council (EPSRC) grants EP/P018998/1, and Special Interests Group of Acoustofluidics under the EPSRC-funded UK Fluidic Network (EP/N032861/1).

APPENDIX A: Effect of SAW device substrate

To see the effect of Rayleigh angle on the contact time of the droplet, here we compare the droplet impact dynamics on ZnO/Al and ZnO/Si SAW devices with the same wavelength. Additionally, as described in the results section, another resistive force is formed due to the CAH along the TPCL. By assuming that the contact area is a complete circle during the impingement, the tangential CAH resistive force, F_{CAH} can be calculated by [59]:

$$F_{CAH} = 24/\pi^3 \gamma_{LV} \delta (cos\theta_{rec} - cos\theta_{adv}) \quad (5)$$

where δ is the base diameter (See FIG. 9 (c)). Newtons second law can be written in the x-direction as:

$$F_{SAW} Sin\theta_R - F_{CAH} - F_v = m dv_x/dt \quad (6)$$

where m is the liquid mass. A few ms before the detachment, δ and TPCL length are significantly reduced (see snapshots in FIG. 9(b)) and thus both resistive forces are minimized. Therefore, the x-component of the SAW force can overcome the resisting forces and drive the droplet along the x-direction before the z-component of the SAW force detaches the whole liquid droplet from the surface. ZnO/Al SAW device, has a lower attenuation constant, compared to the ZnO/Si SAW device. Thus, the x-component of the SAW force is higher which can drive the droplet on the surface in x-direction at high SAW forces before complete detachment. This in turn leads to a change in the contact time for ZnO/Al SAW devices. Since this paper aims to investigate the contact time reduction by using SAWs, we choose to continue our analysis with the ZnO/Si SAW devices.

APPENDIX B: Effect of SAW frequency

To explore the effect of the resonant frequency on droplet impact dynamics, four different SAW devices were fabricated on ZnO/Si surface by changing the structure of the IDTs. Details of the fabricated devices are presented in Table III.

lists the measured frequency of the fabricated ZnO/Al device. The SAW force (see equation 1) is applied to the liquid medium along the Rayleigh angle, and the ratio of the components of the SAW force in x and z directions is equal to the attenuation coefficient ($\frac{F_{SAWz}}{F_{SAWx}} = \alpha_1$) [41]. As shown in Table II, Due to lower sound velocity on the aluminium substrate, the Rayleigh angle is larger for Al-based SAW devices and thus α_1 is lower.

Consequently, the ratio of the $\frac{F_{SAWz}}{F_{SAWx}}$ is lower for the ZnO/Al device compared to the ZnO/Si device due to larger Rayleigh angle. Experimental results of droplet contact time on the surface of ZnO/Al and ZnO/Si SAW devices as a function of SAW amplitude is illustrated in FIG. 9(a). From this graph, we can see that, at lower SAW amplitudes, the contact time for ZnO/Al SAW device is reduced up to 10% on the ZnO/Al device, however by increasing the SAW amplitude ($A/\lambda > 6\times10^{-5}$), the contact time starts to increase sharply. On the other hand, for the ZnO/Si device, the contact time is decreased by increasing the SAW amplitude. The snapshots of the impact show that by applying TSAW to the droplet, it moves a certain distance along the x-direction during the impingement. The transition along the x-direction on the surface before separation, Δx, for both devices is compared in FIG. 9(b). At large SAW amplitudes, Δx is larger for the Al based devices. These results can be explained by further analysis of the forces applied to the liquid. At the given time of *t* after the start of impingement, we analyse the forces along the x-direction to have a better understanding of droplet

transition during the impingement. Due to strain formed along the three-phase contact line for a droplet in motion on a solid surface, a significant viscous force resists droplet motion. Assuming the contact area is circular during the impingement, the viscous resistive force, F_v can be simplified as the liquid surface tension per unit length [17].

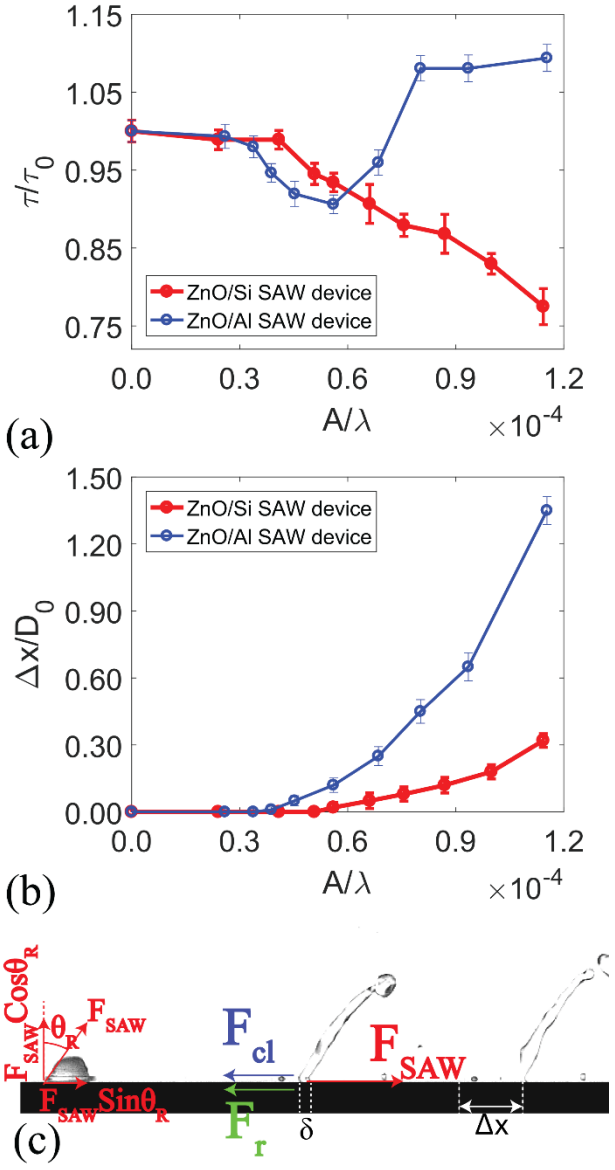

FIG. 9: (a) Experimental results of normalized contact time versus SAW amplitude for ZnO/Si and ZnO/Al SAW devices. For both devices, the wavelength of the SAW is 64 µm, and a droplet with a volume of 3.56 µl is impacting the surface with a velocity of 1.4 m/s. contact time, τ is normalized with the contact time of DFI case, τ_0 for each device. (b) Experimental results of transition distance in x-direction before separation as a function of SAW amplitude. (c) Force analysis of impacting droplet.

Additionally, as described in the results section, another resistive force is formed due to the CAH along the TPCL. By assuming that the contact area is a complete circle during the impingement, the tangential CAH resistive force, F_{CAH} can be calculated by [59]:

$$F_{CAH} = 24/\pi^3 \gamma_{LV} \delta (cos\theta_{rec} - cos\theta_{adv}) \quad (5)$$

where δ is the base diameter (See FIG. 9 (c)). Newtons second law can be written in the x-direction as:

$$F_{SAW} Sin\theta_R - F_{CAH} - F_v = m dv_x/dt \quad (6)$$

where m is the liquid mass. A few ms before the detachment, δ and TPCL length are significantly reduced (see snapshots in FIG. 9(b)) and thus both resistive forces are minimized. Therefore, the x-component of the SAW force can overcome the resisting forces and drive the droplet along the x-direction before the z-component of the SAW force detaches the whole liquid droplet from the surface. ZnO/Al SAW device, has a lower attenuation constant, compared to the ZnO/Si SAW device. Thus, the x-component of the SAW force is higher which can drive the droplet on the surface in x-direction at high SAW forces before complete detachment. This in turn leads to a change in the contact time for ZnO/Al SAW devices. Since this paper aims to investigate the contact time reduction by using SAWs, we choose to continue our analysis with the ZnO/Si SAW devices.

APPENDIX B: Effect of SAW frequency

To explore the effect of the resonant frequency on droplet impact dynamics, four different SAW devices were fabricated on ZnO/Si surface by changing the structure of the IDTs. Details of the fabricated devices are presented in Table III.

Table II: Resonant frequency, Rayleigh angle, SCA, advancing contact angle, receding contact angle and CAH for ZnO/Al SAW device. The contact angles are measured after the surface treatment with CYTOP. The contact time is measured for a 3.56 µl droplet with an impact velocity of 1.41m/s.

SAW Device	Resonant Frequency	Rayleigh Angle	α_1	θ_s	θ_{adv}	θ_{rec}	$\Delta\theta = \theta_{adv} - \theta_{rec}$
ZnO/Al	40.40 (MHz)	34.75°	1.46	114°±2°	114°±1°	105°±1°	9°±2°

To compare the effect of frequency on the dynamics of the impacting droplet, we normalize the SAW wavelength, λ, with the attenuation length of the SAW in the liquid medium, ζ [60].

$$\zeta = \frac{\rho {v_L}^3}{4\pi^2\omega^2(\frac{4}{3}\mu + \mu')} \quad (7)$$

where μ and μ' are the shear and bulk viscosities of the fluid, respectively.

Table III: Measured frequencies and calculated sound velocities and liquid attenuation lengths for ZnO/Si SAW devices

Wavelength (µm)	Frequency (MHz)	$v_s(\frac{m}{s})$	ζ/λ
36	110.82	3989.5	850
64	66.10	4230.4	1602
100	43.12	4312.0	2550
200	22.04	4407.5	5215

The effect of the SAW device resonant frequency on the contact time on the droplet is illustrated in FIG. 10. By increasing the wavelength (i.e. at a higher ζ/λ ratio), SAW propagates longer distances within the liquid medium before significant attenuation. For the devices with a higher resonant frequency, the interaction volume between the SAW and liquid medium is decreased [61]. As a result, less momentum is transferred by SAW to the liquid medium during the impingement. As shown in FIG. 10, the SAW device with a resonant frequency of 110.82 MHz is not capable of significantly reducing the contact time. On the other hand, by effectively transferring the SAW momentum to the droplet during the impingement, the contact time can be significantly reduced by SAW devices with lower resonant frequencies (i.e. 66.10 MHz and lower). However, for the SAW devices with a resonant frequency of 43.12MHz and 22.04 MHz, and at higher SAW amplitudes ($A/\lambda=7\times10^{-5}$ for 43.12MHz device and $A/\lambda=7\times10^{-5}$ for 22.04MHz device), the droplet impact regime can be changed from complete rebound from the surface to break-up. In this case, a few sub-units are separated from the droplet during the retracting phase (See FIG. 10). The mechanism for the droplet break-up can be explained by the attenuation length of the SAW in the liquid medium. At lower frequencies, the attenuation length in the liquid medium is higher, which leads to a higher SAW energy reaching to the liquid-gas interface of the droplet. At larger amplitudes, this energy can overcome the surface tension of the droplet, and the droplet will break into smaller sub-units. Considering the effect of frequency on the droplet behaviour on the surface, we selected to use the SAW devices with a resonant frequency of 66.10 MHz to perform our studies.

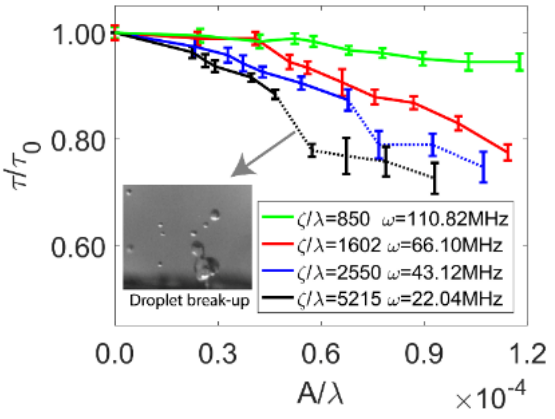

FIG. 10: Experimental results of nnormalized contact time versus wave amplitude for SAW devices with different frequencies for a droplet with a volume of 3.56

μl and impact velocity of 1.4 m/s impacting on the ZnO/Si SAW device surface with CYTOP surface treatment. Solid and dashed lines represent droplet rebounce and break-up regimes, respectively.

APPENDIX C: Dynamic contact angle modelling

As the droplet impingement phenomena in the presence of SAW are asymmetrical, in order to see the internal flow and recirculation inside the droplet, all the numerical simulations are performed in 3D. A boundary condition was developed based on OpenFOAM, which calculate the dynamic contact angles based on Bracke et al. [62] approach

$$\cos\theta_d = \cos\theta_s - (\cos\theta_s + 1).\,K_{DCA}.\,Ca^{0.54} \quad (8)$$

Here the capillary number ($Ca = \mu U_{CL}/\gamma_{LV}$) is defined based on the three-phase contact line velocity, U_{CL} and K_{DCA} was set to 9.63 in all the simulations. More details regarding the CLSVOF method used in simulations are presented in our previous works [52,53].

VII. References

[1] K. Liu, X. Yao, and L. Jiang, Chem. Recent Developments in Bio-Inspired Special Wettability, Soc. Rev. **39**, 3240 (2010).

[2] M. Cao, D. Guo, C. Yu, K. Li, M. Liu, and L. Jiang, Water-Repellent Properties of Superhydrophobic and Lubricant-Infused "Slippery" Surfaces: A Brief Study on the Functions and Applications, ACS Appl. Mater. Interfaces **8**, 3615 (2016).

[3] R. J. Daniello, N. E. Waterhouse, and J. P. Rothstein, Drag Reduction in Turbulent Flows over Superhydrophobic Surfaces, Phys. Fluids **21**, 085103 (2009).

[4] Y. C. Jung and B. Bhushan, Dynamic Effects of Bouncing Water Droplets on Superhydrophobic Surfaces, Langmuir **24**, 6262 (2008).

[5] K. D. Esmeryan, A. H. Bressler, C. E. Castano, C. P. Fergusson, and R. Mohammadi, Rational Strategy for the Atmospheric Icing Prevention Based on Chemically Functionalized Carbon Soot Coatings, Appl. Surf. Sci. **390**, 452 (2016).

[6] L. Mishchenko, B. Hatton, V. Bahadur, J. A. Taylor, T. Krupenkin, and J. Aizenberg, Design of Ice-Free Nanostructured Surfaces Based on Repulsion of Impacting Water Droplets, ACS Nano **4**, 7699 (2010).

[7] C. Clanet, C. Béguin, D. Richard, and D. Quéré, Maximal Deformation of an Impacting Drop, J. Fluid Mech. **517**, 199 (2004).

[8] J. Eggers, M. A. Fontelos, C. Josserand, and S. Zaleski, Drop Dynamics after Impact on a Solid Wall: Theory and Simulations, Phys. Fluids **22**, 062101 (2010).

[9] R. Gupta, V. Vaikuntanathan, and D. Sivakumar, Superhydrophobic Qualities of an Aluminum Surface Coated with Hydrophobic Solution NeverWet, Colloids Surfaces A Physicochem. Eng. Asp. **500**, 45 (2016).

[10] Z. Li, Q. Kong, X. Ma, D. Zang, X. Guan, and X. Ren, Dynamic Effects and Adhesion of Water Droplet Impact on Hydrophobic Surfaces: Bouncing or Sticking, Nanoscale **9**, (2017).

[11] M. Abolghasemibizaki and R. Mohammadi, Droplet Impact on Superhydrophobic Surfaces Fully Decorated with Cylindrical Macrotextures, J. Colloid Interface Sci. **509**, 422 (2018).

[12] B. Ding, H. Wang, X. Zhu, R. Chen, and Q. Liao, Int. Water Droplet Impact on Superhydrophobic Surfaces with Various Inclinations and Supercooling Degrees, J. Heat Mass Transf. **138**, 844 (2019).

[13] Lord Rayleigh, On the Capillary Phenomena of Jets, Proc. R. Soc. London **29**, 71 (1879).

[14] J. C. Bird, R. Dhiman, H. M. Kwon, and K. K. Varanasi, Reducing the Contact Time of a Bouncing Drop, Nature **503**, 385 (2013).

[15] A. Gauthier, S. Symon, C. Clanet, and D. Quéré, Water Impacting on Superhydrophobic Macrotextures, Nat. Commun. **6**, (2015).

[16] Y. Shen, J. Tao, H. Tao, S. Chen, L. Pan, and T. Wang, Approaching the Theoretical Contact Time of a Bouncing Droplet on the Rational Macrostructured Superhydrophobic Surfaces, Appl. Phys. Lett **107**, 111604 (2015).

[17] H. Li, W. Fang, Y. Li, Q. Yang, M. Li, Q. Li, X. Q. Feng, and Y. Song, Droplets Gyrating via Asymmetric Self-Splitting on Heterogeneous Surfaces, Nat. Commun. **10**, (2019).

[18] Y. C. Jung and B. Bhushan, Wetting

Transition of Water Droplets on Superhydrophobic Patterned Surfaces, Scr. Mater. **57**, 1057 (2007).

[19] V. Fink, X. Cai, A. Stroh, R. Bernard, J. Kriegseis, B. Frohnapfel, H. Marschall, and M. Wörner, Drop Bouncing by Micro-Grooves, Int. J. Heat Fluid Flow **70**, 271 (2018).

[20] V. Vaikuntanathan and D. Sivakumar, Maximum Spreading of Liquid Drops Impacting on Groove-Textured Surfaces: Effect of Surface Texture, Langmuir **32**, 2399 (2016).

[21] M. Song, Z. Liu, Y. Ma, Z. Dong, Y. Wang, and L. Jiang, Reducing the Contact Time Using Macro Anisotropic Superhydrophobic Surfaces-Effect of Parallel Wire Spacing on the Drop Impact, NPG Asia Mater. **9**, e415 (2017).

[22] C. Guo, D. Zhao, Y. Sun, M. Wang, and Y. Liu, Droplet Impact on Anisotropic Superhydrophobic Surfaces, Langmuir **34**, 3533 (2018).

[23] C. Guo, D. Maynes, J. Crockett, and D. Zhao, Heat Transfer to Bouncing Droplets on Superhydrophobic Surfaces, Int. J. Heat Mass Transf. **137**, 857 (2019).

[24] B. A. Malouin, N. A. Koratkar, A. H. Hirsa, and Z. Wang, Directed Rebounding of Droplets by Microscale Surface Roughness Gradients, Appl. Phys. Lett. **96**, 1 (2010).

[25] Y. Liu, L. Moevius, X. Xu, T. Qian, J. M. Yeomans, and Z. Wang, Pancake Bouncing on Superhydrophobic Surfaces, Nat. Phys. **10**, 515 (2014).

[26] Y. Liu, G. Whyman, E. Bormashenko, C. Hao, and Z. Wang, Controlling Drop Bouncing Using Surfaces with Gradient Features, Appl. Phys. Lett **107**, 51604 (2015).

[27] J. Song, M. Gao, C. Zhao, Y. Lu, L. Huang, X. Liu, C. J. Carmalt, X. Deng, and I. P. Parkin, Large-Area Fabrication of Droplet Pancake Bouncing Surface and Control of Bouncing State, ACS Nano **11**, 41 (2017).

[28] Y. Liu, M. Andrew, J. Li, J. M. Yeomans, and Z. Wang, Symmetry Breaking in Drop Bouncing on Curved Surfaces, Nat. Commun. **6**, (2015).

[29] S. Jowkar and M. R. Morad, Water Drop Impact on a Semi-Cylindrical Convex Hot Surface for a Diameter Ratio of Unity, Exp. Therm. Fluid Sci. **106**, 68 (2019).

[30] S. Chen and V. Bertola, Drop Impact on Spherical Soft Surfaces, Phys. Fluids **29**, (2017).

[31] Y. Liu, M. Andrew, J. Li, J. M. Yeomans, and Z. Wang, ymmetry Breaking in Drop Bouncing on Curved Surfaces, Nat. Commun. **6**, (2015).

[32] P. B. Weisensee, J. Ma, Y. H. Shin, J. Tian, Y. Chang, W. P. King, and N. Miljkovic, Droplet Impact on Vibrating Superhydrophobic Surfaces, Phys. Rev. Fluids **2**, (2017).

[33] L. Y. Y. and J. R. Friend, Ultrafast Microfluidics Using Surface Acoustic Waves, Biomicrofluidics **3**, (2009).

[34] J. Zhou, H. F. Pang, L. Garcia-Gancedo, E. Iborra, M. Clement, M. De Miguel-Ramos, H. Jin, J. K. Luo, S. Smith, S. R. Dong, D. M. Wang, and Y. Q. Fu, Discrete Microfluidics Based on Aluminum Nitride Surface Acoustic Wave Devices, Microfluid. Nanofluidics **18**, 537 (2015).

[35] A. Zhang, Y. Zha, and J. Zhang, A Surface Acoustic Wave Micropump to Pump Fluids from a Droplet into a Closed Microchannel Using Evaporation and Capillary Effects, Cit. AIP Adv. **4**, (2014).

[36] Z. Wang and J. Zhe, Recent Advances in Particle and Droplet Manipulation for Lab-on-a-Chip Devices Based on Surface Acoustic Waves, Lab Chip **11**, 1280 (2011).

[37] Y. J. Guo, A. P. Dennison, Y. Li, J. Luo, X. T. Zu, C. L. Mackay, P. Langridge-Smith, A. J. Walton, and Y. Q. Fu, Nebulization of Water/Glycerol Droplets Generated by ZnO/Si Surface Acoustic Wave Devices, Microfluid. Nanofluidics **19**, 273 (2015).

[38] T. H. Bui, V. Nguyen, S. Vollebregt, B. Morana, H. van Zeijl, T. Chu Duc, and P. M. Sarro, Effect of Droplet Shrinking on Surface Acoustic Wave Response in Microfluidic Applications, Appl. Surf. Sci. **426**, 253 (2017).

[39] M. Baudoin, P. Brunet, O. B. Matar, and E. Herth, Low Power Sessile Droplets Actuation via Modulated Surface Acoustic Waves, Cit. Appl. Phys. Lett **100**, 154102 (2012).

[40] Y. Q. Fu, J. K. Luo, N. T. Nguyen, A. J. Walton, A. J. Flewitt, X. . Zu, Y. Li, G.

McHale, A. Matthews, E. Iborra, H. Du, and W. I. Milne, Advances in Piezoelectric Thin Films for Acoustic Biosensors, Acoustofluidics and Lab-on-Chip Applications, Prog. Mater. Sci. **89**, 31 (2017).

[41] S. Shiokawa, Y. Matsui, and T. Ueda, Study on Saw Streaming and Its Application to Fluid Devices, Jpn. J. Appl. Phys. **29**, 137 (1990).

[42] S. K. R. S. Sankaranarayanan, S. Cular, V. R. Bhethanabotla, and B. Joseph, Flow Induced by Acoustic Streaming on Surface-Acoustic-Wave Devices and Its Application in Biofouling Removal: A Computational Study and Comparisons to Experiment, Phys. Rev. E - Stat. Nonlinear, Soft Matter Phys. **77**, 1 (2008).

[43] M. Alghane, Y. Q. Fu, B. X. Chen, Y. Li, M. P. Y. Desmulliez, and A. J. Walton, Frequency Effect on Streaming Phenomenon Induced by Rayleigh Surface Acoustic Wave in Microdroplets, J. Appl. Phys. **084902**, (2012).

[44] M. Aminzadeh, A. Maleki, B. Firoozabadi, and H. Afshin, On the Motion of Newtonian and Non-Newtonian Liquid Drops, Sci. Iran. **19**, 1265 (2012).

[45] Š. Šikalo, H. D. Wilhelm, I. V. Roisman, S. Jakirlić, and C. Tropea, Dynamic Contact Angle of Spreading Droplets: Experiments and Simulations, Phys. Fluids **17**, 1 (2005).

[46] M. Sussman and E. G. Puckett, A Coupled Level Set and Volume-of-Fluid Method for Computing 3D and Axisymmetric Incompressible Two-Phase Flows, J. Comput. Phys. **162**, 301 (2000).

[47] S. Afkhami, S. Zaleski, and M. Bussmann, A Mesh-Dependent Model for Applying Dynamic Contact Angles to VOF Simulations, J. Comput. Phys. **228**, 5370 (2009).

[48] S. Yun, Bouncing of an Ellipsoidal Drop on a Superhydrophobic Surface, Sci. Rep. **7**, 17699 (2017).

[49] D. Richard, C. Clanet, and D. Quéré, Surface Phenomena: Contact Time of a Bouncing Drop, Nature **417**, 811 (2002).

[50] Y. Shen, J. Tao, H. Tao, S. Chen, L. Pan, and T. Wang, Relationship between Wetting Hysteresis and Contact Time of a Bouncing Droplet on Hydrophobic Surfaces, ACS Appl. Mater. Interfaces **7**, 20972 (2015).

[51] M. Pasandideh-Fard, Y. M. Qiao, S. Chandra, and J. Mostaghimi, Capillary Effects during Droplet Impact on a Solid Surface, Phys. Fluids **8**, 650 (1996).

[52] M. Jangi, J. T. Luo, R. Tao, J. Reboud, R. Wilson, J. M. Cooper, D. Gibson, and Y. Q. Fu, oncentrated Vertical Jetting Mechanism for Isotropically Focused Zno/Si Surface Acoustic Waves, Int. J. Multiph. Flow **114**, 1 (2019).

[53] M. H. Biroun, M. T. Rahmati, M. Jangi, R. Tao, B. X. Chen, and Y. Q. Fu, Computational and Experimental Analysis of Droplet Transportation/Jetting Behaviours Driven by Thin Film Surface Acoustic Waves, Sensors Actuators, A Phys. **299**, 111624 (2019).

[54] H. Ma, C. Liu, X. Li, H. Huang, and J. Dong, Deformation Characteristics and Energy Conversion during Droplet Impact on a Water Surface, Phys. Fluids **31**, (2019).

[55] A. Bisighini, G. E. Cossali, C. Tropea, and I. V. Roisman, Crater Evolution after the Impact of a Drop onto a Semi-Infinite Liquid Target, Phys. Rev. E **82**, 036319 (2010).

[56] N. Erkan, Full-Field Spreading Velocity Measurement inside Droplets Impinging on a Dry Solid-Heated Surface, Exp. Fluids **60**, 88 (2019).

[57] J. B. Lee, D. Derome, A. Dolatabadi, and J. Carmeliet, Energy Budget of Liquid Drop Impact at Maximum Spreading: Numerical Simulations and Experiments, Langmuir **32**, 1279 (2016).

[58] A. K. Saha, K. Muralidhar, and G. Biswas, Vortex Structures and Kinetic Energy Budget in Two-Dimensional Flow Past a Square Cylinder, Comput. Fluids **29**, 669 (2000).

[59] R. Tao, G. McHale, J. Reboud, J. M. Cooper, H. Torun, J. Luo, J. Luo, X. Yang, J. Zhou, P. Canyelles-Pericas, Q. Wu, and Y. Fu, Hierarchical Nanotexturing Enables Acoustofluidics on Slippery yet Sticky, Flexible Surfaces, Nano Lett. (2020).

[60] W. Connacher, N. Zhang, A. Huang, J. Mei, S. Zhang, T. Gopesh, and J. Friend, Micro/Nano Acoustofluidics: Materials, Phenomena, Design, Devices, and Applications, Lab Chip **18**, 1952 (2018).

[61] Y. J. Guo, H. B. Lv, Y. F. Li, X. L. He, J. Zhou, J. K. Luo, X. T. Zu, A. J. Walton, and

Y. Q. Fu, High Frequency Microfluidic Performance of LiNbO3 and ZnO Surface Acoustic Wave Devices, J. Appl. Phys. **116**, (2014).

[62] N. Fries and M. Dreyer, The Transition from Inertial to Viscous Flow in Capillary Rise, J. Colloid Interface Sci. **327**, 125 (2008).